Monthly Notices
of the
ROYAL ASTRONOMICAL SOCIETY

Mon. Not. R. Astron. Soc. **404,** 1910–1921 (2010) doi:10.1111/j.1365-2966.2010.16402.x

Testing PDR models against *ISO* fine structure line data for extragalactic sources

M. Vasta,[1]★ M. J. Barlow,[1] S. Viti,[1] J. A. Yates[1] and T. A. Bell[2]

[1]*Department of Physics and Astronomy, University College London, Gower Street, London WC1E 6BT*
[2]*Caltech, Department of Physics, MC 320- 47, Pasadena, CA 91125, USA*

Accepted 2010 January 22. Received 2010 January 4; in original form 2009 October 16

ABSTRACT

Far-infrared [C II] 158-μm, [O I] 145-μm and [O I] 63-μm fine structure emission-line fluxes were measured from archival *Infrared Space Observatory* Long Wavelength Spectrometer spectra of 46 extragalactic sources, with 28 sources providing detections in all three lines. For 12 of the sources, the contribution to the [C II] 158-μm line flux from H II regions could be estimated from their detected [N II] 122-μm line fluxes. The measured [C II]/[O I] and [O I] 63/145-μm line flux ratios were compared with those from a grid of photodissociation region (PDR) models previously computed using the UCL_PDR code. Persistent offsets between the observed and modelled line ratios could be partly attributed to the effects of [O I] 63-μm self-absorption. Using the Spherical Multi-Mol (SMMOL) code, we calculated model [O I] line profiles and found that the strength of the [O I] 63-μm line was reduced by 20–80 per cent, depending on the PDR parameters. We conclude that high PDR densities and radiation field strengths, coupled with the effects of [O I] 63-μm self-absorption, are likely to provide the best match to the observed line flux ratios.

Key words: astrochemistry – line: profiles – photodissociation region (PDR) – Galaxy: fundamental parameters – infrared: galaxies.

1 INTRODUCTION

Studies of our own Galaxy and observations of external galaxies have suggested that stellar ultraviolet radiation can ionize vast volumes of a galaxy and that far-ultraviolet (FUV) radiation impinging on neutral cloud surfaces is responsible for a large fraction of the observed far-infrared (FIR) spectral line emission that cools the gas (Crawford et al. 1985). The relative contributions from different gas phases can be estimated from observations of several FIR forbidden lines. Fine structure (FS) emission lines can be used as tracers of nebular conditions such as density, excitation and ionization. By virtue of their different excitation potentials and critical densities, FS emission lines provide an insight into the energetics and chemical composition of the regions from which they originate. The FIR FS lines of abundant species, such as [C II] and [O I], have long been recognized as one of the most important coolants in the interstellar medium. In particular, the emission from singly ionized carbon [C II], at $\lambda = 158\,\mu$m, is known to trace warm and dense photodissociation regions (PDRs) and is used to trace the gas surrounding active star-forming regions. Carbon is the fourth most abundant element and has a lower ionization potential (11.26 eV) than hydrogen. For this reason, it is predominantly in the form of C^+ in the surface layers of PDRs, where photoionization of neutral carbon is effective, but can potentially also be excited in ionized regions. [C II] 158 μm emission is reasonably easy to excite, with a transition energy of 92 K. The line is widely observed and is usually optically thin. The depth of the C^+ zones in neutral clouds is generally determined by dust extinction of carbon ionizing photons and often extends to $A_v \geq 4$, although C^+ decreases in abundance for $A_v \geq 1$ (Bell et al. 2006b).

Another important species is oxygen, which has an ionization potential of 13.62 eV, slightly above that of hydrogen. This means that the ionization structure of $O^+\backslash O^0$ closely follows the ionization structure of hydrogen. Also, the charge exchange of neutral oxygen in two-body recombination with hydrogen cannot be neglected as it affects the ionization balance. The incident FUV radiation maintains a significant abundance of atomic oxygen deep into the cloud through photodestruction of CO and O_2. All oxygen not incorporated into CO can remain in atomic form to depths as large as $A_v = 10$ mag under strong FUV irradiation (Sternberg & Dalgarno 1995). The fraction of oxygen at magnitudes greater than 10 depends on the physical conditions in the cloud (i.e. its density, metallicities and radiation field strength), but essentially if the gas density is $>10^5$ cm^{-3} at these depths, the oxygen not locked in CO is depleted on the grains. However for the purpose of these calculations, the code that we use, UCL_PDR, does not take into account freeze-out reactions. Atomic oxygen has two FS transitions, at 63 and 145 μm. The [O I] line at 63 μm has an excitation energy corresponding to 228 K, is emitted predominantly by warm and dense gas, although

★E-mail: mv@star.ucl.ac.uk

© 2010 The Authors. Journal compilation © 2010 RAS

it can also have an ionized gas component (Aannestad & Emery 2003), and can act as a coolant in neutral hydrogen regions. It may also be a heating agent as O I can heat the gas through the collisional de-excitation of the dust continuum radiation-excited $^3P_1$ FS level (Tielens & Hollenbach 1985). However this mechanism is not well studied. This line is optically thick in some cases (Abel et al. 2007), and its optical depth can be estimated by comparing the [O I] line flux at 63 μm to that of the [O I] line at 145 μm (Abel et al. 2007). The [O I] 145 μm line can be harder to detect: in fact the relative faintness of this line diminishes its capabilities as a robust PDR diagnostic. The lower level of the 145 μm line is not the ground state of O^0, meaning that [O I] 145 μm emission is usually optically thin (Abel et al. 2007). The 145 μm line has an excitation energy of 326 K, almost 100 K higher than that of the 63 μm line, so the ratio of the two line intensities is sensitive to the gas temperature for $T \leq 300$ K. Since the strength of the FUV radiation field governs the heating of the gas, this line ratio is also a diagnostic of the incident FUV flux (Tielens & Hollenbach 1985).

In the presence of foreground cold and tenuous gas, the [O I] 63 μm line can show both emission and absorption components (Tielens & Hollenbach 1985; González-Alfonso et al. 2004; Liseau, Justtanont & Tielens 2006). Nevertheless observations of the FIR FS emission lines of [O I] and [C II] can be used as diagnostics to infer the physical conditions in the emitting gas, such as temperatures, densities and radiation field strengths, by comparing with models of PDRs (Tielens & Hollenbach 1985) and H II regions (Rubin et al. 1991). In the past, several models have been used to interpret infrared, submillimetre and millimetre line observations of neutral gas in our own Galaxy as well as in the central regions of nearby starburst galaxies (e.g. Wild et al. 1992, and references therein; Mao et al. 2000; Seaquist & Frayer 2000).

In this paper, we will use FIR line fluxes measured from the *Infrared Space Observatory* (*ISO*) archive for a sample of extragalactic sources. We present the fluxes of FS emission lines observed by *ISO* from 46 sources, and we estimate the bulk properties of the gas in these external galaxies using the UCL_PDR model of Bell et al. (2005) and the radiative transfer code Spherical Multi-Mol code (SMMOL) (Rawlings & Yates 2001).

The paper is structured as follows. In Section 2, we give details of the sources selected and the FS emission-line fluxes we measured. In Section 3, we describe the UCL_PDR models. In Section 4, we evaluate the sensitivity of the UCL_PDR models to variations in the physical parameters. In Section 5, we will consider the contribution of H II regions to FS emission lines. The results are given in Section 6, and there we discuss their interpretation in the context of our SMMOL line profile calculations. Concluding remarks are given in Section 7.

2 THE *ISO* DATA

All the FIR data included in this paper were acquired using the *ISO* Long Wavelength Spectrometer (LWS; Clegg et al. 1996), which had an estimated FWHM beam size of ∼80 arcsec.

We collected [C II]158, [O I]145 and 63 μm emission-line fluxes from *ISO* LWS archival observations for 46 external galaxies. The [C II]158, [O I]145 and 63 μm emission-line fluxes were measured from the spectra using the interactive package Spectroscopy Modelling Analysis and reduction Tool (SMART; Higdon et al. 2004.)

Table 1 lists the emission-line fluxes measured by us from the *ISO* spectra. For 33 of the galaxies, fluxes previously published in the literature were available and these are also listed in Table 1. When uncertainties were not listed for these literature fluxes, we have estimated them as 20 per cent for fluxes $\leq 10^{-14}$ W m^{-2} and 10 per cent for fluxes $\geq 10^{-14}$ W m^{-2}. Although the choice of how to estimate the associated errors, when it is not provided, is arbitrary, we used typical uncertainties resulting from calibration and pointing errors in the Submillimetre and IR domain (Israel, White & Baas 1995; Bayet et al. 2004; Martín, Martín-Pintado & Mauersberger 2006). The percentage uncertainty estimated in this way appears, on average, to be similar to the percentage line flux uncertainties measured by us using the interactive package SMART.

In order to show that our measurements are in good agreement with the fluxes collected from the literature, we have plotted our measurements versus literature values in Fig. 1. We have plotted the ratio of the literature value of $[C\,II]_{158}/[O\,I]_{63}$ over our own measured $[C\,II]_{158}/[O\,I]_{63}$ value, with respective error bars (open triangles), as well as the ratio of the literature value of $[O\,I]_{63}/[O\,I]_{145}$ over our own value of $[O\,I]_{63}/[O\,I]_{145}$, with respective error bars (filled triangles). The horizontal line in Fig. 1 represents the case in which the literature ratios and our own measured ratios are in perfect agreement.

Flux ratios of two lines of the same species, such as $[O\,I]_{145}/[O\,I]_{63}$, can provide information about nebular conditions such as temperature (or radiation field strength). In addition, a ratio such as $[O\,III]_{88}/[O\,III]_{52}$ can provide information on the electron density. In addition by using ratios, rather than fitting the line intensities directly, the beam filling factors of the two emission lines cancel out, assuming that they come from the same regions and are of the same size.

Fig. 2 shows the $[C\,II]_{158}/[O\,I]_{63}$ ratio versus the $[O\,I]_{63}/[O\,I]_{145}$ ratio for the 28 sources, out of the 46 listed in Table 1, that showed $\geq 4\sigma$ detections in all three lines.

3 THE UCL_PDR MODELS

We used the UCL_PDR time and depth-dependent PDR code (Bell et al. 2006a) which solves the chemistry, thermal balance and radiative transfer self-consistently within a cloud. The range of parameter values input to the code is listed in Table 2, including the mean grain radius and grain number density adopted for grain surface reactions. The FUV grain opacity properties adopted by UCL_PDR are listed by Bell et al. (2006b). The outputs of the code are the abundances of each species included in the chemical network, their column densities, the emissivities and integrated intensities of the emission lines involved in the cooling and the gas and dust temperatures. All of these quantities are functions of depth and time. At each depth step, the model calculates the attenuation of the FUV field before beginning an iterative cycle to determine the gas temperature at which the total heating and cooling rates are equal, that is, when the condition of thermal balance is satisfied. For each iteration, the chemistry is first calculated, based on the gas temperature and attenuated FUV flux, after which the heating and cooling rates are computed, together with the radiative transfer in the emission line, using the revised chemical abundances. The difference between the total heating and cooling rates is then used to derive a new gas temperature. We use a grid of 1702 PDR models, already computed and partially used in previous works (Bell et al. 2006a,b; Bell et al. 2007) spanning a large range of densities, metallicities and cosmic ray ionization rates. Amongst the range of parameter values covered by the grid of models (see Table 2), we do not consider variations of the turbulent velocity parameter in our attempts to fit the observed emission from each galaxy, since the line ratios are believed to be fairly insensitive to small changes in the turbulent velocity (Wolfire, Hollenbach & Tielens 1989).

© 2010 The Authors. Journal compilation © 2010 RAS, MNRAS **404,** 1910–1921

Table 1. Line flux measurements, in units of 10^{-14} W m^{-2}, for extragalactic sources with *ISO*-LWS detections of all three FIR FS emission lines of [C II] and [O I]. For each source, our own line flux measurements are listed in the first row, while literature values, if any, are listed in the second row (Fischer et al. 1996; Colbert et al. 1999; Bergvall et al. 2000; Unger et al. 2000; Malhotra et al. 2001; Negishi et al. 2001; Contursi et al. 2002; Luhman et al. 2003; Brauher, Dale & Helou 2008) (n.a: not available).

Index	Source	Radial Velocity (km s^{-1})	TDT No. of Observation	[C II] 158 μm	[O I] 63 μm	[O I] 145 μm	[C II]$_{158}$ / [O I]$_{63}$	[O I]$_{63}$ / [O I]$_{145}$
1	**IC 10**	−348	45700609	0.966 ± 0.034	0.591 ± 0.025	0.0217 ± 0.0032	1.64 ± 0.13	27.23 ± 5.17
				0.763 ± 0.021	0.65 ± 0.02	0.024 ± 0.004	1.17 ± 0.07	27.08 ± 5.34
2	**Haro 11**	6175	54900720	0.0410 ± 0.0022	0.0954 ± 0.0041	<0.0086	0.43 ± 0.04	n.a
				0.039 ± 0.001	0.092 ± 0.018	0.003 ± 0.001	0.42 ± 0.09	30.6 ± 16.2
3	**NGC 253**	243	56901708	4.618 ± 0.126	3.47 ± 0.16	0.461 ± 0.074	1.33 ± 0.09	7.53 ± 1.55
				5.19 ± 1.04	3.76 ± 0.75	0.52 ± 0.11	1.38 ± 0.55	7.23 ± 2.97
4	**NGC 520**	2281	77702295	0.2188 ± 0.0045	0.29 ± 0.015	0.0133 ± 0.0028	0.75 ± 0.05	21.80 ± 5.72
				0.28 ± 0.06	0.21 ± 0.04	0.02 ± 0.01	1.33 ± 0.54	10.5 ± 7.3
5	**Maffei 2**	−17	85800682	1.072 ± 0.051	0.512 ± 0.051	0.071 ± 0.021	2.09 ± 0.31	7.21 ± 2.85
				1.21 ± 0.24	0.53 ± 0.11	0.05 ± 0.01	2.28 ± 0.93	10.6 ± 4.3
6	**NGC 1068**	1137	60500401	1.881 ± 0.062	1.416 ± 0.043	0.1522 ± 0.0024	1.33 ± 0.08	9.30 ± 0.43
				2.13 ± 0.43	1.60 ± 0.32	0.09 ± 0.02	1.33 ± 0.54	17.8 ± 7.5
7	**IC 342**	31	64600302	0.3146 ± 0.0097	<0.117	0.0202 ± 0.0049	n.a	n.a
				n.a	n.a	n.a	n.a	n.a
8	**NGC 1482**	1916	79600984	0.571 ± 0.022	0.362 ± 0.025	<0.057	1.58 ± 0.17	n.a
				0.655 ± 0.013	0.318 ± 0.063	n.a	2.06 ± 0.45	n.a
9	**NGC 1569**	-104	64600489	0.652 ± 0.027	0.657 ± 0.025	0.0085 ± 0.0019	0.99 ± 0.08	77.3 ± 20.2
				0.674 ± 0.134	0.589 ± 0.119	n.a	1.14 ± 0.46	n.a
10	**NGC 1614**	4778	85501010	0.1953 ± 0.0067	0.346 ± 0.016	0.0179 ± 0.0026	0.56 ± 0.05	19.33 ± 3.70
				0.226 ± 0.010	0.343 ± 0.016	n.a	0.65 ± 0.05	n.a
11	**NGC 2146**	893	67900165	2.479 ± 0.078	1.756 ± 0.091	0.164 ± 0.023	1.41 ± 0.12	10.70 ± 2.06
				2.62 ± 0.52	1.73 ± 0.35	0.10 ± 0.02	1.51 ± 0.61	17.3 ± 6.7
12	**NGC 2388**	4134	71802360	0.1473 ± 0.0073	0.0954 ± 0.0058	0.0032 ± 0.0010	1.54 ± 0.17	29.81 ± 11.13
				0.191 ± 0.038	0.097 ± 0.019	n.a	1.97 ± 0.77	n.a
13	**M 82**	203	65800611	13.02 ± 0.30	16.70 ± 0.59	1.366 ± 0.056	0.78 ± 0.05	12.23 ± 0.93
				12.79 ± 2.59	16.94 ± 3.38	1.46 ± 0.29	0.75 ± 0.31	11.60 ± 4.62
14	**NGC 3256**	2804	25200456	1.124 ± 0.044	1.178 ± 0.033	<0.032	0.95 ± 0.03	n.a
				1.37 ± 0.27	1.28 ± 0.26	n.a	1.07 ± 0.43	n.a
15	**IRAS 10565 +2448**	12921	20200453	0.0551 ± 0.0076	0.0848 ± 0.0069	<0.011	0.65 ± 0.14	n.a
				0.047 ± 0.009	0.076 ± 0.008	n.a	0.61 ± 0.18	n.a
16	**NGC 3620**	1680	27600981	0.173 ± 0.012	0.152 ± 0.093	< 0.046	1.14 ± 0.77	n.a
				0.249 ± 0.049	0.164 ± 0.029	0.029 ± 0.006	1.52 ± 0.57	5.65 ± 2.17
17	**NGC 3690**	3121	18000704	0.755 ± 0.028	0.895 ± 0.084	0.074 ± 0.012	0.84 ± 0.11	12.09 ± 3.10
				0.86 ± 0.17	0.83 ± 0.17	0.05 ± 0.005	1.03 ± 0.41	16.6 ± 5.1
18	**NGC 4039/9**	1641	25301107	0.378 ± 0.011	0.412 ± 0.079	0.0211 ± 0.0041	0.92 ± 0.20	19.53 ± 7.54
				0.37 ± 0.01	0.34 ± 0.07	n.a	1.09 ± 0.25	n.a
19	**NGC 4102**	846	19500584	0.322 ± 0.012	0.341 ± 0.022	0.0141 ± 0.0041	0.944 ± 0.096	24.18 ± 8.59
				0.289 ± 0.049	0.269 ± 0.049	0.022 ± 0.004	1.07 ± 0.38	12.22 ± 4.45
20	**NGC 4151**	995	35800185	0.0551 ± 0.0043	0.401 ± 0.032	0.0331 ± 0.0047	0.14 ± 0.02	12.11 ± 2.71
			35300163	0.074 ± 0.006	0.376 ± 0.029	n.a	0.19 ± 0.031	n.a
21	**NGC 4194**	2501	19401369	0.2094 ± 0.0073	0.267 ± 0.010	<0.0057	0.78 ± 0.06	n.a
				0.217 ± 0.008	0.28 ± 0.02	0.013 ± 0.003	0.77 ± 0.08	21.53 ± 6.50
22	**NGC 4449**	207	23400120	0.2383 ± 0.0086	0.151 ± 0.046	0.0187 ± 0.0044	1.58 ± 0.53	8.07 ± 4.36
				0.278 ± 0.008	0.133 ± 0.013	n.a	2.09 ± 0.26	n.a
23	**NGC 4490**	565	20501578	0.430 ± 0.014	0.333 ± 0.017	<0.0063	1.29 ± 0.11	n.a
				0.423 ± 0.084	0.328 ± 0.065	0.011 ± 0.002	1.29 ± 0.51	29.81 ± 11.33
24	**NGC 4670**	1609	58000205	0.0954 ± 0.0083	0.717 ± 0.075	0.0248 ± 0.0051	0.13 ± 0.03	28.91 ± 8.97
				0.094 ± 0.008	<1.13	<0.17	n.a	n.a
25	**NGC 4945**	563	28000446	3.547 ± 0.075	1.82 ± 0.061	0.38 ± 0.021	1.95 ± 0.11	4.79 ± 0.43
				3.52 ± 0.70	1.93 ± 0.39	0.34 ± 0.07	1.82 ± 0.73	5.67 ± 2.31
26	**Cen A**	547	63400464	2.764 ± 0.085	1.757 ± 0.068	0.102 ± 0.0062	1.57 ± 0.11	17.23 ± 1.71
				2.90 ± 0.58	1.92 ± 0.39	0.10 ± 0.02	1.51 ± 0.61	19.2 ± 7.74
27	**NW Cen A**	547	45400151	2.79 ± 0.22	0.984 ± 0.070	0.0744 ± 0.0058	2.83 ± 0.43	13.22 ± 1.97
				2.43 ± 0.48	0.90 ± 0.18	0.08 ± 0.02	2.7 ± 1.1	11.25 ± 5.06
28	**M 51**	600	35100651	0.951 ± 0.048	0.623 ± 0.057	0.0268 ± 0.0038	1.53 ± 0.22	23.25 ± 5.42
				1.04 ± 0.01	0.44 ± 0.09	n.a	2.36 ± 0.51	n.a
29	**M 83**	513	64200513	1.202 ± 0.051	1.37 ± 0.29	0.137 ± 0.032	0.88 ± 0.22	10.0 ± 4.45
				1.76 ± 0.35	1.18 ± 0.24	0.10 ± 0.02	1.49 ± 0.60	11.8 ± 4.8

Table 1 – *continued*

Index	Source	Radial Velocity (km s^{-1})	TDT No. of Observation	[C II] 158 μm	[O I] 63 μm	[O I] 145 μm	$[C\,II]_{158}$ $[O\,I]_{63}$	$[O\,I]_{63}$ $[O\,I]_{145}$
30	**Circinus**	434	10401133	2.61 ± 0.10	2.170 ± 0.084	0.1606 ± 0.023	1.20 ± 0.09	3.58 ± 0.27
				2.65 ± 0.53	2.30 ± 0.46	0.18 ± 0.05	1.15 ± 0.46	12.77 ± 6.10
31	**Mrk 297**	4739	62702069	0.227 ± 0.027	0.291 ± 0.037	<0.19	0.78 ± 0.19	n.a
				0.21 ± 0.008	0.225 ± 0.18	<0.18	0.93 ± 0.78	n.a
32	**NGC 6240**	7339	27801108	0.2447 ± 0.0082	0.651 ± 0.027	0.0349 ± 0.0029	0.38 ± 0.03	18.65 ± 2.32
				0.29 ± 0.06	0.69 ± 0.14	0.031 ± 0.007	0.42 ± 0.17	22.26 ± 9.54
33	**NGC 6810**	2031	84700610	0.311 ± 0.014	0.22 ± 0.031	<0.016	1.41 ± 0.26	n.a
				0.40 ± 0.08	0.18 ± 0.04	n.a	2.22 ± 0.93	n.a
34	**NGC 6946**	48	45700139	0.876 ± 0.028	0.611 ± 0.024	<0.061	1.43 ± 0.10	n.a
				1.03 ± 0.21	0.59 ± 0.12	0.05 ± 0.01	1.74 ± 0.71	11.8 ± 4.8
35	**NGC 7673**	3408	76601364	0.1061 ± 0.0041	0.172 ± 0.041	<0.0075	0.62 ± 0.17	n.a
				n.a	n.a	n.a	n.a	n.a
36	**Mrk 331**	5541	56500637	0.182 ± 0.006	0.096 ± 0.008	0.0076 ± 0.0018	1.89 ± 0.22	12.63 ± 4.03
				0.148 ± 0.008	0.11 ± 0.006	<0.13	1.34 ± 0.14	n.a
37	**NGC 4151**	995	35300163	0.822 ± 0.006	0.445 ± 0.024	<0.042	1.85 ± 0.11	n.a
				0.074 ± 0.006	0.37 ± 0.029	n.a	0.20 ± 0.03	n.a
38	**NGC 6286**	5501	20700509	0.187 ± 0.008	0.087 ± 0.004	0.0094 ± 0.0013	2.15 ± 0.19	9.25 ± 1.70
				0.168 ± 0.005	0.073 ± 0.009	0.005 ± 0.001	2.30 ± 0.35	14.6 ± 4.7
39	**NGC 6574**	2282	70500604	0.436 ± 0.021	0.223 ± 0.034	0.078 ± 0.017	1.95 ± 0.39	2.86 ± 1.05
				0.44 ± 0.020	0.23 ± 0.041	n.a	1.91 ± 0.42	n.a
40	**NGC 6822**	-57	34300915	0.176 ± 0.011	0.128 ± 0.005	0.008 ± 0.002	1.37 ± 0.15	16.5 ± 3.9
				0.187 ± 0.011	0.143 ± 0.006	<0.05	1.30 ± 0.13	n.a
41	**NGC 7552**	1608	36903087	0.583 ± 0.028	0.20 ± 0.04	0.037 ± 0.007	2.92 ± 0.72	5.41 ± 2.10
				0.64 ± 0.015	0.63 ± 0.023	n.a	1.01 ± 0.06	n.a
42	**NGC 7771**	4277	56500772	0.29 ± 0.01	0.141 ± 0.009	0.0187 ± 0.0026	2.06 ± 0.20	7.54 ± 1.52
				0.298 ± 0.009	0.115 ± 0.013	n.a	2.59 ± 0.37	n.a
43	**NGC 4041**	1234	22202506	0.32 ± 0.01	0.38 ± 0.05	<0.14	0.84 ± 0.13	n.a
				0.348 ± 0.005	0.197 ± 0.016	n.a	1.76 ± 0.16	n.a
44	**NGC 0278**	627	59702260	0.72 ± 0.002	<0.03	0.020 ± 0.002	n.a	n.a
				0.728 ± 0.012	0.347 ± 0.016	<0.021	2.09 ± 0.13	n.a
45	**NGC 0695**	9735	63300744	0.137 ± 0.007	0.19 ± 0.01	0.010 ± 0.002	0.72 ± 0.07	19 ± 4.8
				0.20 ± 0.008	0.118 ± 0.009	n.a	1.69 ± 0.19	n.a
46	**NGC 0986**	1974	74300187	0.278 ± 0.009	0.19 ± 0.04	0.013 ± 0.001	1.46 ± 0.35	14.62 ± 4.20
				0.304 ± 0.011	0.127 ± 0.013	<0.025	2.39 ± 0.33	n.a

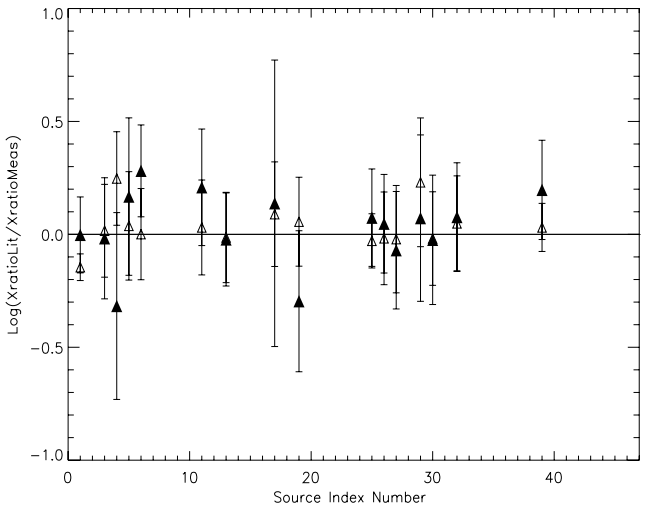

Figure 1. $[C\,II]_{158}/[O\,I]_{63}$ and $[O\,I]_{63}/[O\,I]_{145}$ ratios. Filled triangles represent the ratio of the literature value of $[O\,I]_{63}/[O\,I]_{145}$ over our own measured $[O\,I]_{63}/[O\,I]_{145}$ ratio, with respective error bars. Open triangles represent the ratio of the literature value of $[C\,II]_{158}/[O\,I]_{63}$ over our own measured $[C\,II]_{158}/[O\,I]_{63}$ ratio with respective error bars. The horizontal line represents the case in which literature ratios and our own measured ratios are perfectly matched. The source index numbers and galaxy identifications are listed in Table 1.

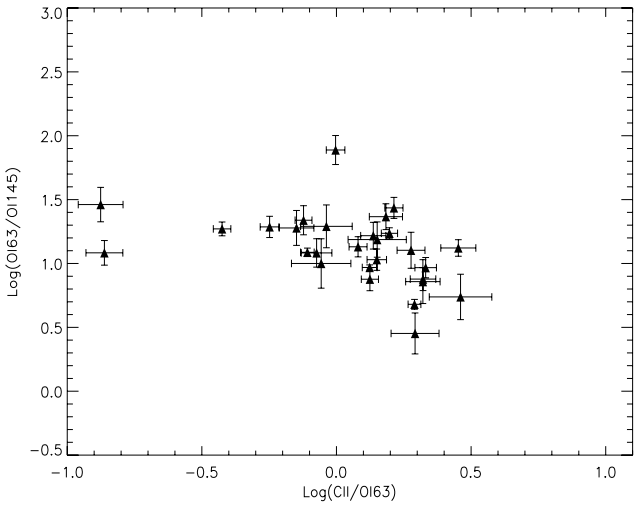

Figure 2. The observed $[C\,II]_{158}/[O\,I]_{63}$ ratios versus the $[O\,I]_{63}/[O\,I]_{145}$ ratios for detections $\geq 4\sigma$, with error bars.

4 SENSITIVITY OF MODEL RESULTS TO PARAMETER VARIATIONS

We attempted to find the range of physical parameters which best reproduced the observations, such as visual extinction, metallicity,

Table 2. Physical and chemical parameters for the UCL_PDR grid. In the grid of models the density and the radiation field parameters are incremented by 2 dex and 1 dex, respectively.

Parameter	Range of values	Reference parameter values
Cloud density (cm^{-3})	$10^2 \leq n_H \leq 10^5$	$n_H = 10^3$
Incident FUV flux (Habing)	$10 \leq G_0 \leq 10^5$	$G_o = 10$
Age of the cloud (yr)	$10^4 \leq t \leq 10^8$	$t = 10^7$
Cloud size (mag)	$0 \leq A_v \leq 10$	$A_v = 10$
Metallicity	$Z/Z_\odot$ = 5,4,3,2,1,0.5 0.1,0.25,0.01	$Z = Z_\odot$
C.R. ionization rate (s^{-1})	$\zeta = 5\times, 50\times, 500 \times 10^{-15}$ $5\times, 50\times, 500 \times 10^{-16}$ $5\times, 50\times, 500 \times 10^{-17}$	$\zeta = 5 \times 10^{-17}$
Turbulent velocity (km s^{-1})	$v_{turb} = 1.5$	$v_{turb} = 1.5$
Carbon elemental abundance	$1.4 \times 10^{-4} n_H$	Sofia & Myer (2001)
Oxygen elemental abundance	$3.2 \times 10^{-4} n_H$	Sofia & Myer (2001)
Grain radius	0.1 μm	0.1 μm
Grain number density n_g	$2 \times 10^{-12} Z\, n\ cm^{-3}$	$2 \times 10^{-9}\ cm^{-3}$

cosmic ray ionization rate and UV radiation field strength. The influence of changing the number density of hydrogen nuclei (n_H), the visual extinction (A_v), the incident radiation field strength (G_o), the cosmic ray ionization rate ζ and the metallicity (Z) is considered individually by varying only one of these parameters at a time. The age of the modelled regions was set to a value of 10^7 yr, owing to the fact that clouds with ages $\geq 10^7$ yr do not undergo significant changes in their predicted chemical profiles, even though, in some cases, the chemistry only reaches its final steady state somewhat later (Bell et al. 2006b).

When one parameter was varied, the remainder were held constant at the reference parameter values listed in the final column of Table 2.

In Figs 3 through 8, we overplot our model predictions against flux ratios from the [C II] 158 μm and [O I] 63 and 145 μm *ISO* LWS fluxes. Table 3 lists these three important PDR cooling transitions, their wavelengths, upper energy levels E_{upper} and critical densities

Table 3. PDR diagnostic transitions. The critical densities for [C II] and [O I] are for collisions with H (Tielens & Hollenbach 1985).

Species	Transitions	Wavelength (μm)	E_{upper}/k (K)	n_{cr} (cm^{-3})
[C II]	$^2P_{3/2}$–$^2P_{1/2}$	157.74	92	3×10^3
[O I]	$^3P_1$–$^3P_2$	63.18	228	4.7×10^5
[O I]	$^3P_0$–$^3P_1$	145.53	326	1×10^5

n_{cr}. In this section, we will only discuss the sensitivity of the ratios to changes in the input parameters. The comparison with observations will be made in Section 6.

4.0.1 *Visual extinction*

PDRs derive their properties primarily from the penetration of FUV photons into their interiors. Dust grains provide the major source of continuum opacity and attenuate the incident radiation field by selectively absorbing and scattering light at visible and ultraviolet wavelengths. This means that there is a strong correlation between visual extinction and the chemistry of PDRs. We examined models for different visual extinction values in the range $1 \leq A_v \leq 10$. From Fig. 3, one can see that there is no significant change in the emission-line ratios from $A_v = 1$ (black circle) to $A_v = 10$ (green circle). This trend implies that the majority of the line fluxes arises from $1 \leq A_v \leq 2$ and is consistent with the C^+ abundance because, for values of A_v larger than 2, this ion recombines to form C^0 and subsequently forms CO. Indeed C^+ is a tracer of the edge of PDRs. This implies that the C^+ FS emission lines that are observed are coming predominantly from regions with low visual extinction. Although neutral oxygen is still present at higher visual extinctions, it is somewhat reduced beyond $A_v = 1$ because a fraction of oxygen combines with C to form CO (see Röllig et al. 2007). We fixed $A_v = 10$ as the most appropriate depth range to fit our sample of sources, since Fig. 3 shows that we cannot distinguish between models with optical depths in the range of $1 \leq A_v \leq 10$.

4.0.2 *Radiation field*

Radiation field strengths incident upon a gas cloud can vary from the standard interstellar field (χ = Draine) up to $\chi \sim 10^7$ Draines

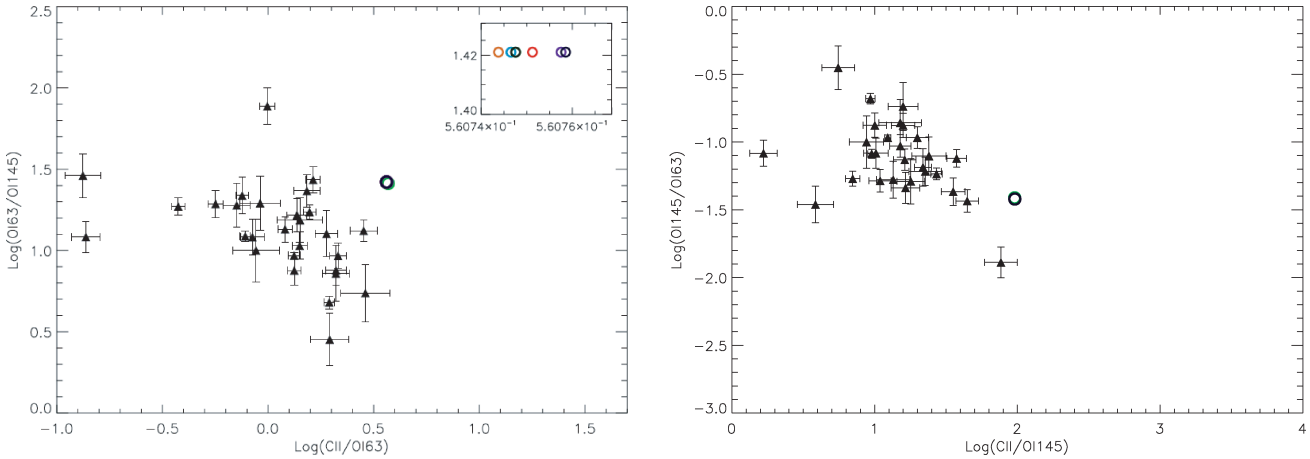

Figure 3. $[C\,II]_{158}/[O\,I]_{63}$ versus $[O\,I]_{63}/[O\,I]_{145}$ ratios (left-hand panel) and $[C\,II]_{158}/[O\,I]_{145}$ versus $[O\,I]_{145}/[O\,I]_{63}$ ratios (right-hand panel), with error bars, compared with models of varying visual extinctions. The insert, in the left-hand panel, shows a zoomed-in region of the overlapping coloured circles corresponding to differing visual extinction values.

© 2010 The Authors. Journal compilation © 2010 RAS, MNRAS **404,** 1910–1921

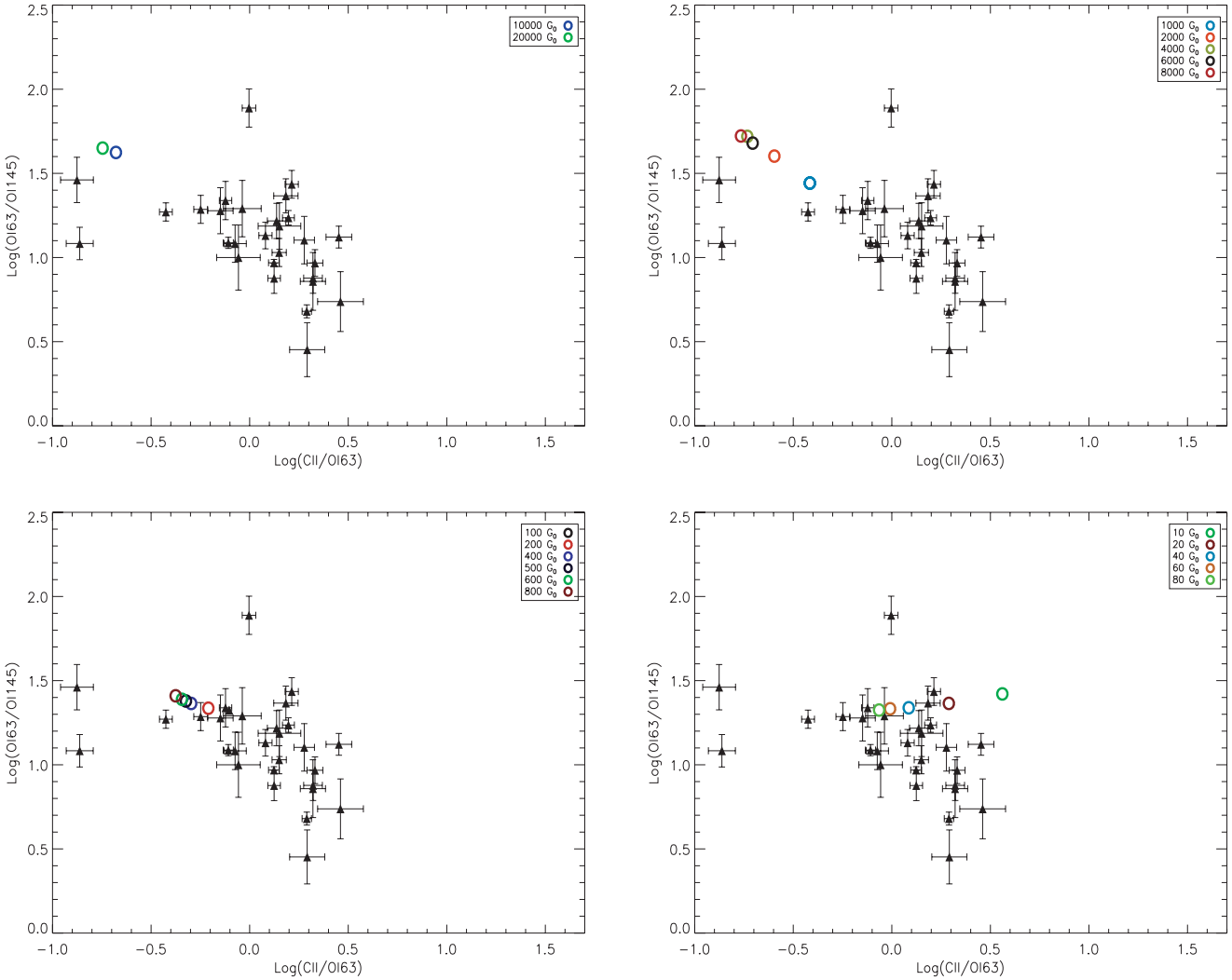

Figure 4. The four panels show observed $[\mathrm{C\,II}]_{158}/[\mathrm{O\,I}]_{63}$ versus $[\mathrm{O\,I}]_{63}/[\mathrm{O\,I}]_{145}$ ratios, with uncertainties. In the top-left panel the coloured circles represent models with radiation field strengths in the range $10^4 \leq G_0 \leq 2 \times 10^4$. In the top-right panel the coloured circles represent models with radiation field strengths in the range $10^3 \leq G_0 \leq 8 \times 10^3$. In the bottom-left panel the coloured circles represent models with radiation field strengths in the range $10^2 \leq G_0 \leq 8 \times 10^2$. In the bottom-right panel the coloured circles represent models with radiation field strengths in the range $10 \leq G_0 \leq 80$.

(Draine 1978) in regions of intense star formation (see Hollenbach & Tielens 1997). The FUV field may be also expressed in terms of the Habing parameter (Habing 1968). The FUV flux expressed in this way is determined by the parameter $G_0 = \chi/1.7$. We adopt a range of $10 \leq G_0 \leq 500\,000$ Habings for consideration in this study, but we only plot the significant results. From Fig. 4, $[\mathrm{C\,II}]_{158}/[\mathrm{O\,I}]_{63}$ versus $[\mathrm{O\,I}]_{63}/[\mathrm{O\,I}]_{145}$ appears to be sensitive to variations in the radiation field strength. As the radiation field strength increases so does the $[\mathrm{O\,I}]_{63}/[\mathrm{O\,I}]_{145}$ ratio, while the $[\mathrm{C\,II}]_{158}/[\mathrm{O\,I}]_{63}$ ratio decreases. The energy required to excite the $[\mathrm{O\,I}]_{63}$ transition is somewhat higher than that for $[\mathrm{C\,II}]_{158}$, hence the line intensity ratio $[\mathrm{O\,I}]_{63}/[\mathrm{C\,II}]_{158}$ is expected to increase with gas temperature and hence higher FUV flux. PDR models predict that for $n_{\mathrm{H}} > 10^3$ cm^{-3} the line ratio will increase with both G_0 and n_{H}, due to the different critical densities of the two transitions (Wolfire, Tielens & Hollenbach 1990).

4.0.3 Metallicity

Metallicities significantly below solar are observed in Local Group galaxies, including the Small Magellanic Cloud (SMC), as well as in more distant dwarf galaxies, with I Zw 18's metallicity of 1/40 being amongst the lowest known (Izotov & Thuan 1999). The metallicity dependence appears in several key processes in the UCL_PDR code. Elemental abundances of all metals are assumed to scale linearly with metallicity ($Z/Z_{\odot}$); the dust-to-gas mass ratio is also assumed to scale linearly with metallicity and takes a standard value of 10^{-2} at solar metallicity. The formation rate of H_2 on grain surfaces and the grain photoelectric heating rate are assumed to scale linearly with metallicity.

We investigated a metallicity range of $0.01 \leq Z/Z_{\odot} \leq 5$ for this study, with the adopted solar neighbourhood carbon and oxygen elemental abundances listed in Table 2. Metallicity affects the total abundances of carbon and oxygen bearing species and hence can influence the chemical and thermal structure of PDRs in galaxies.

In Fig. 5, we show our model results for metallicities of 0.01 (light green circle), 0.25 (claret circle) and 0.5 (turquoise circle), with remaining symbols representing values of one, two, three, four and five times solar metallicity, respectively.

The C/O ratios for the Sun, the Large Magellanic Cloud and the SMC are all ∼0.5 within the uncertainties, but for lower metallicities

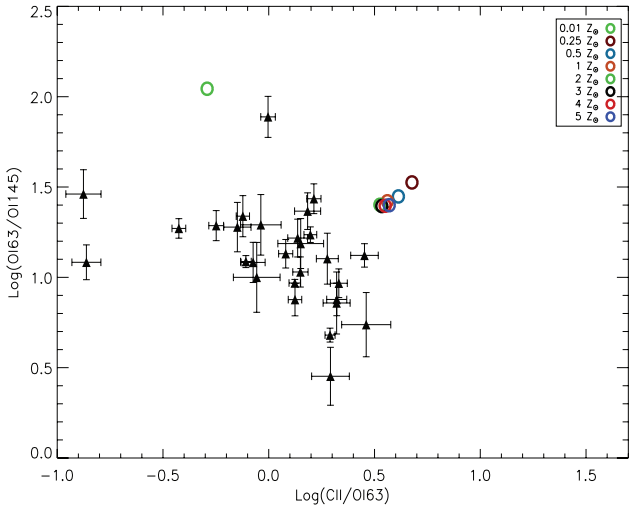

Figure 5. Observed $[C\,II]_{158}/[O\,I]_{63}$ versus $[O\,I]_{63}/[O\,I]_{145}$ ratios, with uncertainties, compared to models of differing metallicity. The coloured circles represent models with different values of metallicity, ranging from 0.01 (light green circle), 0.25 (claret circle) and 0.5 (turquoise circle) up to five times solar metallicity.

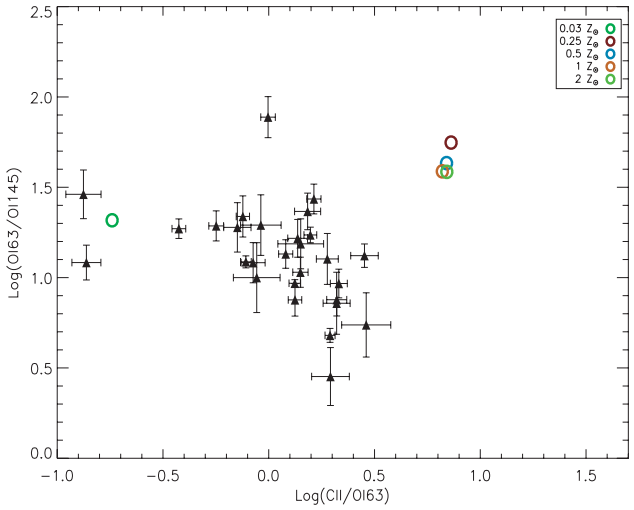

Figure 6. Observed $[C\,II]_{158}/[O\,I]_{63}$ versus $[O\,I]_{63}/[O\,I]_{145}$ ratios, with uncertainties, compared to models of differing metallicity, with the C/O ratio adopted to be 0.53 for metallicities of 0.25 and above, but dropping to 0.16 as metallicities decrease to 0.03. The coloured circles represent models with different values of metallicity, ranging from 0.03 (light green circle), 0.25 (claret circle) and 0.5 (turquoise circle) up to twice solar metallicity.

than the SMC C/H decreases faster than O/H. We tried to reproduce this trend by changing carbon and oxygen elemental abundances with metallicity. In Fig. 6, we show our model results for a metallicity of $Z/Z_\odot = 1$, with C/O = 0.53 (Asplund et al. 2005), then we scale all the elemental abundances with $Z/Z_\odot$ down to $Z/Z_\odot = 0.25$. Below $Z/Z_\odot = 0.25$, the C/O ratio was scaled from 0.53 to 0.16 as $Z/Z_\odot$ was reduced from 0.25 to 0.03 (Izotov & Thuan 1999). As expected, the $[O\,I]_{63}/[O\,I]_{145}$ ratio is not sensitive to variations of metallicity whereas the $[C\,II]_{158}/[O\,I]_{63}$ ratio would appear at first sight to be a good tracer of metallicity.

4.0.4 *Density*

We have considered the sensitivity of the FS emission-line intensities to H-nuclei densities in the range $10^2 \leq n_H \leq 10^5\,cm^{-3}$. In Fig. 7, we show our model results for different values of density. The $[C\,II]_{158}/[O\,I]_{63}$ and $[O\,I]_{63}/[O\,I]_{145}$ ratios are both sensitive to density; however, there is a higher sensitivity for the $[C\,II]_{158}/[O\,I]_{63}$ ratio. As expected, there is a substantial decline in the $[O\,I]_{63}/[O\,I]_{145}$ ratio as the density decreases from $n_H \sim 10^5\,cm^{-3}$ to $n_H \sim 9 \times 10^3\,cm^{-3}$ and a steady decline in the $[O\,I]_{63}/[O\,I]_{145}$ ratio as the density decreases from $n_H \sim 9 \times 10^3$ while the model $[C\,II]_{158}/[O\,I]_{63}$ ratios increase initially with decreasing density until the density reaches a value of $n_H \sim 10^3\,cm^{-3}$ and then decrease as the density decreases further. Clearly, the changes in the $[O\,I]_{63}/[O\,I]_{145}$ ratio at $10^5\,cm^{-3}$ are partly due to the critical density of the two lines (see Table 3). Similarly, the decrease in the $[C\,II]_{158}/[O\,I]_{63}$ ratio as the density decreases is partially due to the density falling below the critical density of the $[C\,II]_{158}$ line.

4.0.5 *Cosmic ray ionization rate*

The cosmic ray flux is known to vary by over an order of magnitude in the Milky Way (Schilke et al. 1993). Magnetic field lines can channel cosmic rays away from dense molecular cores; alternatively, the flux of particles in star-forming regions can be many times higher than the canonical rate (Schilke et al. 1993). The UCL_PDR code does not have a separate treatment for X-ray dominated region (XDR) effects that may be important in some galaxies (see Meijerink, Spaans & Israel 2006). However, to a first approximation, one may use an enhanced cosmic ray ionization rate to mimic the effects of XDRs (Bell et al. 2006a). In Fig. 8, we show our model results for cosmic ray ionization rates in the range $5 \times 10^{-15} \leq \zeta \leq 5 \times 10^{-17}\,s^{-1}$. The higher end of our range can represent a higher ionization rate (see e.g. McCall et al. 2003) or the effect of additional ionization due to X-rays. There is a substantial decline in the $[O\,I]_{63}/[O\,I]_{145}$ ratio as the cosmic ray ionization rate decreases from $\zeta = 5 \times 10^{-15}\,s^{-1}$ (green circle) to $\zeta = 5 \times 10^{-16}\,s^{-1}$ (claret circle) and it then decreases slightly for $\zeta = 5 \times 10^{-17}\,s^{-1}$ (blue circle); the $[C\,II]_{158}/[O\,I]_{63}$ ratio decreases significantly from $\zeta = 5 \times 10^{-15}\,s^{-1}$ (green circle) to $\zeta = 5 \times 10^{-16}\,s^{-1}$ (claret circle) and then remains constant. In fact, both the [C II] and $[O\,I]_{63}$ fluxes decrease with a decrease in ionization rate, with $[O\,I]_{63}$ decreasing at a faster rate.

5 USING [N II] FLUXES TO ESTIMATE THE IONIZED GAS CONTRIBUTION TO [C II] FLUXES

Several studies have been made that show that significant [C II] emission can arise from H II regions (Heiles 1994; Abel et al. 2005; Abel 2006; Kaufman, Wolfire & Hollenbach 2006). Since the ionization potential from C^+ to C^{2+} is 24 eV, the [C II] 158 μm $^2P_{3/2}$ to $^2P_{1/2}$ line can be formed over a substantial part of an H II region and according to Aannestad & Emery (2003) may contribute up to 1/3 of the total intensity in the line.

More recent work has indicated that approximately 25 per cent of the observed [C II] 158 μm emission may come from ionized regions (Abel 2006). This is particularly true where low-density H II regions are adjacent to PDRs (Heiles 1994; Abel et al. 2005; Kaufman et al. 2006; Abel et al. 2007). This effect can hamper the use of [C II] emission as a pure PDR diagnostic in cases where ionized and PDR

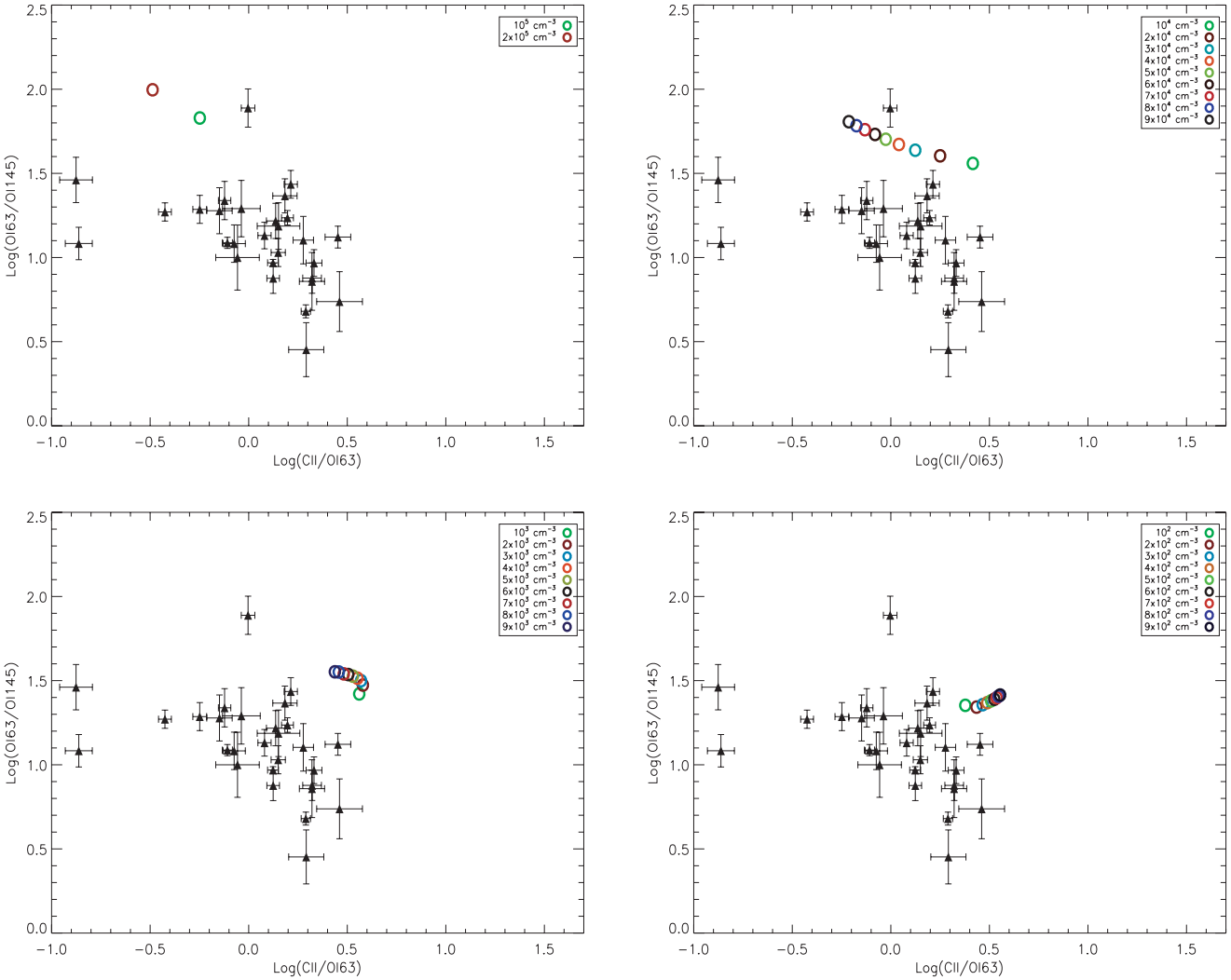

Figure 7. Observed $[\mathrm{C\,II}]_{158}/[\mathrm{O\,I}]_{63}$ versus $[\mathrm{O\,I}]_{63}/[\mathrm{O\,I}]_{145}$ ratios, with uncertainties, compared to models of differing densities. In the top-left panel the coloured points represent models with densities in the range $10^5 \leq n_{\mathrm{H}} \leq 2 \times 10^5\,\mathrm{cm}^{-3}$ decreasing from left to right. In the top-right panel, the coloured points represent models with density values in the range $10^4 \leq n_{\mathrm{H}} \leq 9 \times 10^4\,\mathrm{cm}^{-3}$, decreasing from left to right. In the bottom-left panel, the coloured points represent models with densities in the range $10^3 \leq n_{\mathrm{H}} \leq 9 \times 10^3\,\mathrm{cm}^{-3}$ decreasing from left to right. In the bottom-right panel the coloured points represent models with density values in the range $10^2 \leq n_{\mathrm{H}} \leq 9 \times 10^2\,\mathrm{cm}^{-3}$, decreasing from right to left.

emission are observed in a single spectrum. Therefore, the contribution of [C II] emission from the ionized gas must be estimated. Such an estimate requires a separate model of the H II region, although in recent years computational methods exist that allow the H II region and PDR spectrum to be calculated self-consistently (Abel et al. 2005; Kaufman et al. 2006). A study of S125 by Aannestad & Emery (2003) found that ∼40 per cent of the [C II] and ∼20 per cent of the [O I] 63-μm line intensities come from the ionized regions. Therefore, even though [C II] emission is widely observed and is usually optically thin, its dependence on the properties of the H II region can diminish its use as a PDR diagnostic. The possibility that some of the [C II] flux may come from H II regions is not explicitly taken into account by the UCL_PDR models.

While ionized carbon, because of its ionization potential, can be found in both neutral gas and ionized gas clouds, species such as ionized nitrogen, N^+, requiring an ionization potential of 14.53 eV, can arise only from H II regions. Along with the [C II] 158-μm emission line, the [N II] 122-μm and 205-μm lines are the brightest emission lines contributing to the total FIR emission from our Galaxy (Wright et al. 1991). The ground state ^{3}P term of the N^+ ion is split into the three $^3P_{2,1,0}$ levels from which the 122-μm and 205-μm lines arise. Therefore, if a predicted H II region value for the $[\mathrm{C\,II}]_{158}/[\mathrm{N\,II}]_{122}$ flux ratio is available, the observed [N II] 122-μm flux could be used to indicate the amount of [C II] 158-μm emission arising from H II regions that are in the telescope beam.

The *COBE* Far Infrared Absolute Spectrophotometer Galactic plane spectral measurements yielded an integrated value of $[\mathrm{N\,II}]_{122}/[\mathrm{N\,II}]_{205} = 1.5$ (Wright et al. 1991). The same $[\mathrm{N\,II}]_{122}/[\mathrm{N\,II}]_{205}$ flux ratio was measured by Oberst et al. (2006) for the Great Carina nebula, which has $N_e \sim 30\ \mathrm{cm}^{-3}$. They used photoionization models for the Carina nebula to estimate $[\mathrm{C\,II}]_{158}/[\mathrm{N\,II}]_{122} = 1.6$ for the H II region. Table 4 lists the [N II] 122-μm emission-ine fluxes measured by us from the *ISO* LWS spectra of 12 out of the 46 sources listed in Table 1 that showed a detection, together with the relative $[\mathrm{C\,II}]_{158}/[\mathrm{N\,II}]_{122}$ ratios and the estimated percentage of $[\mathrm{C\,II}]_{158}$ coming from the H II region. The

© 2010 The Authors. Journal compilation © 2010 RAS, MNRAS **404,** 1910–1921

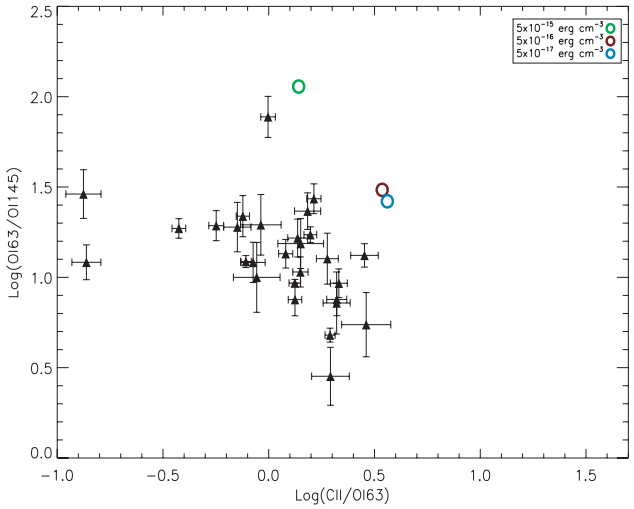

Figure 8. Observed $[C\,II]_{158}/[O\,I]_{63}$ versus $[O\,I]_{63}/[O\,I]_{145}$ ratios, with uncertainties, compared to models with differing cosmic ray ionization rates. The coloured circles represent models with cosmic ray ionization rates of $\zeta = 5 \times 10^{-15}\,s^{-1}$ (green circle), $\zeta = 5 \times 10^{-16}\,s^{-1}$ (claret circle) and $\zeta = 5 \times 10^{-17}\,s^{-1}$ (blue circle).

12 sources that have detections of both [C II] 158 and [N II] 122 μm have mean and median $[C\,II]_{158}/[N\,II]_{122}$ flux ratios of 10.2 and 5.9, respectively. An H II region $[C\,II]_{158}/[N\,II]_{122}$ ratio of 1.6 implies that H II regions contribute only 16 per cent (mean case) and 27 per cent (median case) of the overall [C II] 158 μm flux that is observed.

We used the above predicted H II region $[C\,II]_{158}/[N\,II]_{122}$ ratio of 1.6 along with the observed [N II] 122-μm fluxes to correct the observed [C II] 158-μm flux of these 12 sources for H II region contributions. In Fig. 9, we overplot our model results, with the same physical parameters used in Fig. 4, on the observations. In the right-hand panel, the observations have been corrected for the predicted H II region contribution to the 158-μm fluxes using the measured [N II] 122-μm fluxes. As shown in Fig. 9, the model results appear to fit the corrected observations better, compared to Fig. 4, because the observations have been shifted to lower values of $[C\,II]_{158}/[O\,I]_{63}$. The remaining discrepancy is attributed to [O I] 63-μm self-absorption, as discussed in Section 6 below.

6 FITTING THE OBSERVATIONS

The clear discrepancy between the location of the observations and our models in Figs 3–8 can at least be partly attributed to self-absorption in the [O I] 63-μm line. This is consistent with what Liseau et al. (2006) found, namely that ∼65 per cent of observed $[O\,I]_{63}/[O\,I]_{145}$ emission-line ratios from Milky Way PDRs are lower than can be explained by current models, which they attributed to optical depth effects in the [O I] 63-μm line. They partially attributed the low observed ratios to absorption by cold foreground O^0 in front of the 63-μm-emitting region, although other explanations such as very optically thick [O I] line emission could not be ruled out.

The overall conclusion of Liseau et al. (2006) was that because this ratio depends sensitively on models, [O I] emission has a limited diagnostic value. In fact, most PDR models calculate the emergent flux from a plane-parallel slab of gas illuminated from one side. A galaxy has many PDRs at all orientations, and optical depth effects are non-negligible. In the approximation that the densest PDRs correspond to the shells of molecular clouds and that the [C II] line emission and far-IR dust continuum emission are optically thin, while the [O I] 63-μm line is optically thick, the [O I] 63-μm line will be seen only from the front side of each cloud while the [C II] line arises from both the front and the near sides. The velocity dispersion from cloud to cloud, however, allows most [O I] 63-μm photons that have escaped their parent cloud to escape the galaxy entirely. This scenario implies that we should observe only a fraction of the [O I] flux and all of the [C II] flux expected from PDR models (Malhotra et al. 2001).

The observed $[C\,II]_{158}/[O\,I]_{63}$ and $[O\,I]_{63}/[O\,I]_{145}$ ratios, in the selected range, do not appear to be traced properly by our UCL_PDR model results although there is a common trend in the behaviour of these ratios, indicating that the observations are offset compared to our model results. At first glance the model in the lower right hand panel of Fig. 4, where we varied the radiation field strength, appears to show the best fit to the observations. However, taking into account the effects of [O I] self-absorption and the [C II] contribution from H II regions, the models in the lower left hand panel of Fig. 4 could also probably provide a fit to the observations. In fact, both these effects would shift the models downwards and to the right relative to the observations. A similar trend could be found when we varied the density. Although at first glance the models in the top-right panel of Fig. 7 do not appear to show a good fit to the

Table 4. Line flux measurements, in units of 10^{-14} W m^{-2}, for extragalactic sources with *ISO*-LWS detections of the [N II] 122-μm emission line, together with the observed $[C\,II]_{158}/[N\,II]_{122}$ flux ratio. Column 1 is the index number from Table 1.

Index	Source	TDT No. of Observation	[N II] 122 μm	$[C\,II]_{158}$ $[N\,II]_{122}$	$[C\,II]_{158}$ from H II (per cent)
3	**NGC 253**	56901708	1.72 ± 0.18	2.7 ± 0.4	∼60
5	**Maffei 2**	85800682	0.188 ± 0.014	5.7 ± 0.7	∼28
6	**NGC 1068**	60500401	0.356 ± 0.026	5.3 ± 0.6	∼30
10	**NGC 1614**	85501010	0.021 ± 0.004	9.7 ± 2.5	∼17
11	**NGC 2146**	67900165	0.152 ± 0.006	16.3 ± 6.4	∼10
13	**M 82**	65800611	2.20 ± 0.17	5.9 ± 0.6	∼27
18	**NGC 4039/9**	25301107	0.0468 ± 0.0049	8.08 ± 1.09	∼20
26	**Cen A**	63400464	0.170 ± 0.019	16.2 ± 2.4	∼10
27	**NW Cen A**	45400151	0.097 ± 0.011	28.8 ± 5.7	∼5.5
28	**M 51**	35100651	0.228 ± 0.027	4.2 ± 0.7	∼38
29	**M 83**	64200513	0.231 ± 0.066	5.2 ± 1.7	∼31
30	**Circinus**	10401133	0.213 ± 0.019	12.2 ± 1.5	∼13

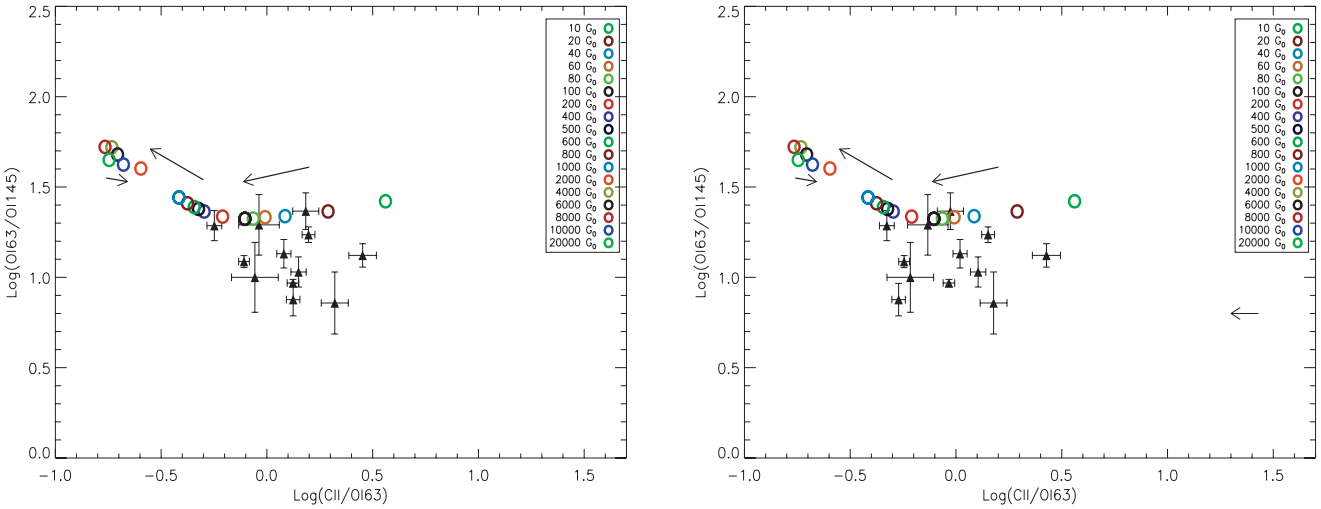

Figure 9. Observed $[\mathrm{C\,II}]_{158}/[\mathrm{O\,I}]_{63}$ versus $[\mathrm{O\,I}]_{63}/[\mathrm{O\,I}]_{145}$ ratios, with uncertainties. In the left-hand panel, the observations do not take into account the likely percentage of [C II] coming from H II regions, while in the right-hand panel the estimated contribution to the [C II] flux is taken into account for each source. The coloured points represent models with radiation field strengths in the range $10 \leq G_0 \leq 2 \times 10^4$ and the arrows indicate the direction of the increase of radiation field strength. The arrow on the right-hand side of the right-hand panel corresponds to the median shift in the $[\mathrm{C\,II}]_{158}/[\mathrm{N\,II}]_{122}$ ratio, corresponding to 27 per cent of the [C II] emission originating from H II regions (see Section 5).

observations, if one takes into account the effects of $[\mathrm{O\,I}]_{63}$ self-absorption, which will shift observations downwards and to the left relative to the models, due to the decrease in the [O I] 63-μm flux, these models will probably provide a better fit to the observations. The models will be shifted downwards and to the right relative to the observations. Unfortunately, the results obtained varying the cosmic ray ionization rate and the metallicity suggest that the $[\mathrm{C\,II}]_{158}/[\mathrm{O\,I}]_{63}$ versus $[\mathrm{O\,I}]_{63}/[\mathrm{O\,I}]_{145}$ ratio is not a good tracer for these parameters. We identified the best parameter values of our source sample as $10^4 \leq n_{\mathrm{H}} \leq 9 \times 10^4$ cm^{-3} and $60 \leq G_0 \leq 8 \times 10^2$, $A_{\mathrm{v}} = 10$. These values were chosen while taking into account the effects of absorption in the [O I] 63-μm line (see Section 6.1) and the contribution to [C II] 158-μm from H II regions (Section 5).

6.1 [O I] 63-μm self-absorption

The intensity of the [O I] 63-μm line can be suppressed through self-absorption. (e.g. González-Alfonso et al. 2004). The $^3\mathrm{P}_1$ state, the upper level of the [O I] 63-μm line, is 228 K above the ground state and its critical density is $n_{\mathrm{crit}} = 4.7 \times 10^5$ cm^{-3} (Tielens & Hollenbach 1985). Because of this, at typical interstellar cloud temperatures all oxygen atoms occupy the lowest level of their ground state, with $J = 2$. This means that [O I] 63-μm emission, originating from collisional excitation in a warm medium, could be absorbed by the abundant reservoir of ground state neutral oxygen that exists within the galaxy along the line of sight. The 63-μm line can also be absorbed by cold foreground material but this is less likely in the case of a face-on galaxy, where the neutral oxygen column density will be less along the line of sight than for an edge-on galaxy. For our sample of sources, the majority is not edge-on galaxies, therefore we attribute most of the suppression of the [O I] 63-μm line to self-absorption in the PDRs in which the emission is excited.

6.1.1 The [O I] 63-μm line profile

In an attempt to investigate the effect of [O I] 63-μm self-absorption on the observations we have developed a new version of the SMMOL (Rawlings & Yates 2001). Originally SMMOL only considered a sphere of material illuminated by the standard ISRF at the outer boundary of the sphere: we have now implemented the ability to insert a central illuminating source with an arbitrary spectral energy distribution. SMMOL uses an accelerated Λ-iteration method to solve multilevel non-local thermodynamic equilibrium radiative transfer problems of gas inflow and outflow. The code computes the total radiation field and the level populations self-consistently. At each radial point, SMMOL generates the level populations, the line source functions and the emergent spectrum from the cloud surface. This can then be convolved with the appropriate telescope beam. A detailed description of the SMMOL radiative transfer model can be found in the appendix of Rawlings & Yates (2001). The coupling between the UCL_PDR code and the radiation transfer code has been performed through an interface[1] that will be presented in a forthcoming paper (Bayet et al., in preparation). We used the physical parameters from one of the UCL_PDR models[2] and we chose an arbitrary distance of 3.2 Mpc for the clouds modelled. In Fig. 10, we show the SMMOL [O I] emission-line profiles for a PDR with a diameter of 20 pc (left-hand panel) and a PDR with a diameter of 5 pc (right-hand panel). In Fig. 10, the effect of self-absorption is clearly seen in the $[\mathrm{O\,I}]_{63\,\mu\mathrm{m}}$ line profile (solid line) while there is no trace of self-absorption in the $[\mathrm{O\,I}]_{145\,\mu\mathrm{m}}$ line profile (dotted line). The $[\mathrm{O\,I}]_{63\,\mu\mathrm{m}}$ emission line is still significantly brighter than the $[\mathrm{O\,I}]_{145\,\mu\mathrm{m}}$ emission line, consistent with current observations. The line profile from a single 20 pc giant molecular cloud (GMC) exhibits extremely strong [O I] 63-μm self-absorption. Without self-absorption in the [O I] 63-μm line, the 63/145 flux ratio would be 46.2. With self-absorption, the flux ratio is found to be 8.5, a reduction of 0.73 dex. The effect is smaller for the 5 pc model; the 63/145 flux ratio is reduced from 12.6 to 7.9, i.e. by 0.20 dex. The log(63/145) ∼ 0.9 flux ratios predicted by both SMMOL models are

[1] See website: https://www.astro.uni-koeln.de/projects/schilke/sites/www.astro.uni-koeln.de.projects.schilke/files/Viti_Cologne09.pdf.

[2] Model result listed in Fig. 4 (bottom left panel): $\zeta = 5 \times 10^{-17}$ s^{-1}, 10^3 cm^{-3}, $Z/Z_{\odot} = 1$, $200G_0$ and $t = 10^7$ yr.

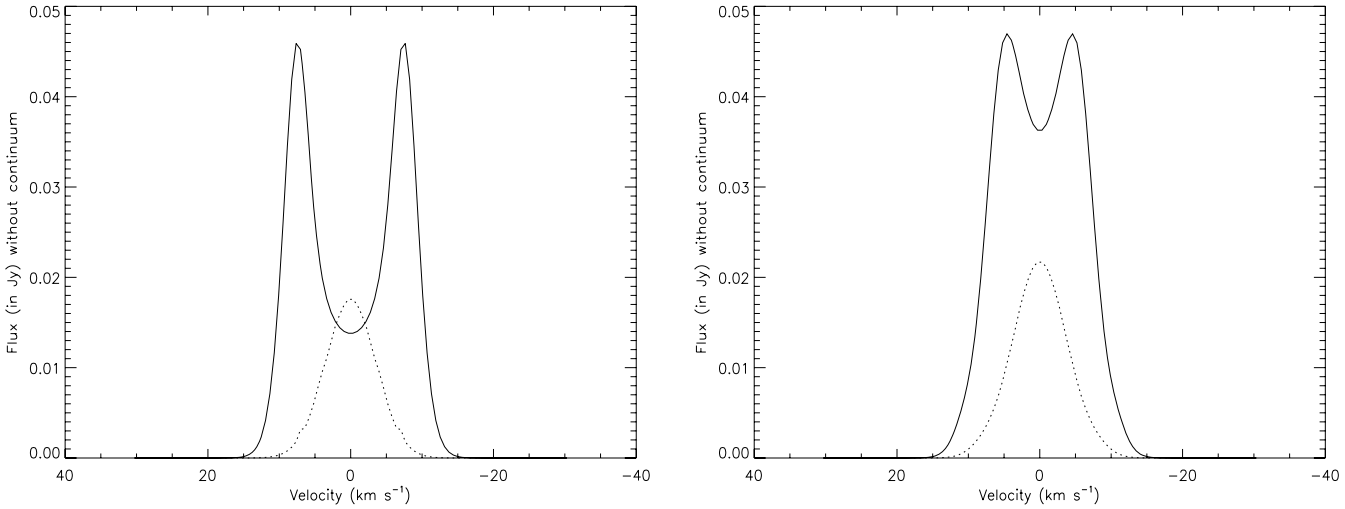

Figure 10. Theoretical oxygen line profiles produced from a 20 pc GMC (left-hand panel) and from a 5 pc GMC (right-hand panel), observed at a distance of 3.2 Mpc. The dotted line represents the [O I]$_{145\,\mu m}$ emission-line profile and the solid line represents the [O I]$_{63\,\mu m}$ emission-line profile. The physical parameters of the UCL_PDR model used for modelling the oxygen line profiles were $\zeta = 5 \times 10^{-17}$ s^{-1}, 10^3 cm^{-3}, $Z/Z_\odot = 1$, $200G_0$ and $t = 10^7$ yr.

in reasonable agreement with the observed ratios in, e.g., Fig. 9. Although our 20 and 5 pc diameter SMMOL models produce similar final 63- and 145-μm fluxes, their relative masses (1.0×10^5 and 1.6×10^3 M$_\odot$, respectively) would seem to make an ensemble of the smaller clouds more plausible for matching the observed ratios.

Note that although all profiles in Fig. 10 have been modelled with the same physical parameters, the difference between the two [O I]$_{63\,\mu m}$ emission-line profiles is due to the difference between the inner and outer temperatures of the two clouds. The 20-pc GMC is approximately 100 K cooler than the 5-pc GMC at the centre. This is because the 20-pc GMC extends to $A_v = 19$ mag, while the 5-pc GMC has a visual extinction of ∼5 mag. These differences account for the much stronger [O I]$_{63\,\mu m}$ self-absorption in the left-hand panel. The [O I]$_{145\,\mu m}$ line, on the other hand, is approximately the same for both GMCs.

In order to qualitatively understand the behaviour of [O I]$_{63\,\mu m}$ self-absorption in PDRs, we investigated its sensitivity to variations in the density and radiation field strength. We find that an order of magnitude increase in the radiation field strength causes the inner and outer temperatures to be twice as high as those in the models plotted in Fig. 10. This produces a higher flux and an increase in self-absorption in the [O I]$_{63\,\mu m}$ line. Increasing the density by one order of magnitude causes an increase in the optical depth of the cloud, so that the degree of [O I]$_{63\,\mu m}$ self-absorption is larger than in the right-hand panel of Fig. 10, while the overall flux is reduced by an order of magnitude. We underline here that we are not attempting to model the actual line profiles that may be exhibited by these galaxies: in order to do so one would need to consider density gradients, multiple sources and the geometry of the galaxy. Our theoretical line profiles simply demonstrate the effect of the initial conditions on the degree of self-absorption in the [O I]$_{63\,\mu m}$ line.

The [O I] 63/145 flux ratios predicted by our SMMOL models shift them downwards by 0.2–0.7 dex relative to the UCL_PDR predictions, bringing them into quite good agreement with the observed ratios plotted in Figs 9 and 10. However, allowance for the 0.2–0.7-dex reduction in the [O I] 63-μm line strength caused by self-absorption would also move the UCL_PDR [C II]/[O I]$_{63\,\mu m}$ model ratios in those figures to larger values. We ran SMMOL for the case of C^+ and we found, as expected, that the [C II]$_{158\,\mu m}$ emission-line profile did not show self-absorption in any of the models. In summary, we find that 20–80 per cent of the intensity of the [O I]$_{63\,\mu m}$ line can be suppressed through absorption, with the percentage depending strongly on the physical parameters of the PDR region. Comparing with the model trends shown in Fig. 9, it would seem that a combination of high radiation field strengths and allowance for [O I] 63-μm self-absorption could provide the best match to the observed line ratios. [O I] line profile observations from the *Herschel Space Observatory* should allow a greater degree of discrimination amongst possible models.

7 CONCLUSIONS

To fit the observed [C II] 158-μm, [O I] 63-μm and [O I] 145-μm emission-line fluxes for 28 extragalactic sources, measured from archival *ISO*-LWS spectra, we used a grid of 1702 PDR models from the UCL_PDR code spanning a large range of densities, radiation field strengths, metallicities and cosmic ray ionization rates. We took into account the contribution to the observed [C II] fluxes from H II regions, using expected [C II]$_{158}$/[N II]$_{122}$ ratios for H II regions to correct the [C II]$_{158}$ fluxes of the 12 sources that had [N II] 122-μm detections.

We found that the best-fitting PDR models had $10^4 \leq n_H \leq 9 \times 10^4$ cm^{-3} and $60 \leq G_0 \leq 8 \times 10^2$. Consistent with the conclusions of Liseau et al. (2006), we found that the persistent discrepancy between the observed and modelled line flux ratios can at least partly be attributed to self-absorption in the [O I] 63-μm line. We used the SMMOL code to predict oxygen emission-line profiles for several PDR models and found clearly self-absorbed [O I] 63-μm profiles, with 20–80 per cent of the intensity suppressed, depending on the physical parameters of the PDR regions. A combination of high radiation field strengths and [O I] self-absorption would appear to provide the best explanation for the observed [C II] 158-μm, [O I] 63-μm and [O I] 145-μm line flux ratios.

ACKNOWLEDGMENTS

We thank the referee, Dr N. Abel, for constructive comments that helped improve the paper. MV would like to thank Dr Estelle Bayet

© 2010 The Authors. Journal compilation © 2010 RAS, MNRAS **404,** 1910–1921

for her help throughout this research. Samuel Farrens is thanked for comments.

REFERENCES

Aannestad P. A., Emery R. J., 2003, A&A, 406, 155
Abel N. P., 2006, MNRAS, 368, 1949
Abel N. P., Ferland G. J., Shaw G., van Hoof P. A. M., 2005, ApJ, 161, 65
Abel N. P., Sarma A. P., Troland T. H., Ferland G. J., 2007, ApJ, 662, 1024
Asplund M., Grevesse N., Sauval A. J., Allende Prieto C., Blomme R., 2005, A&A, 431, 693
Bayet E., Gerin M., Phillips T. G., Contursi A., 2004, A&A, 427, 45
Bell T. A., Viti S., Williams D. A., Crawford I. A., Price R. J., 2005, MNRAS, 357, 961
Bell T. A., Hartquist T. W., Viti S., Williams D. A., 2006a, A&A, 459, 805
Bell T. A., Roueff E., Viti S., Williams D. A., 2006b, MNRAS, 371, 1865
Bergvall N., Masegosa J., Östlin G., Cernicharo J., 2000, A&A, 359, 41
Brauher J. R., Dale D. A., Helou G., 2008, ApJS, 178, 280
Clegg P. E., Ade P. A. R., Armand C., Baluteau J.-P., Barlow M. J., Buckley M. A., Berges J.-C., 1996, A&A, 315, L38
Colbert J. W. et al., 1999, ApJ, 511, 721
Contursi A. et al., 2002, ApJ, 124, 751
Crawford M. K., Genzel R., Townes C. H., Watson D. M., 1985, ApJ, 291, 755
Draine B. T., 1978, ApJ, 36, 595
Fischer J., Shier L. M., Luhman M. L., Satyapal S., Smith H. A., Stacey G. J., Unger S. J., 1996, A&A, 315, L97
González-Alfonso E., Smith H. A., Fischer J., Cernicharo J., 2004, ApJ, 613, 247
Habing H. J., 1968, Bull. Astron. Inst. Netherlands, 19, 421
Heiles C., 1994, ApJ, 436, 720
Higdon S. J. U., Devost D., Higdon J. L., Brandl B. R., Houck J. R., Hall P., 2004, PASP, 116, 975
Hollenbach D. J., Tielens A. G. G. M., 1997, ARA&A, 35, 179
Israel F. P., White G. J., Baas F., 1995, A&A, 302, 343
Izotov Y. I., Thuan T. X., 1999, ApJ, 511, 639
Kaufman M. J., Wolfire M. G., Hollenbach D. J., 2006, ApJ, 644, 283
Liseau R., Justtanont K., Tielens A. G. G. M., 2006, A&A, 446, 561
Luhman M. L., Satyapal S., Fischer J., Wolfire M. G., Sturm E., Dudley C. C., Lutz D., Genzel R., 2003, ApJ, 594, 758
McCall B. J., Huneycutt A. J., Saykally R. J., Geballe T. R., Djuric N., Dunn G. H., 2003, Nat, 422, 500
Malhotra S. et al., 2001, ApJ, 561, 766
Mao R. Q., Henkel C., Schulz A., Zielinsky M., Mauersberger R., Störzer H., Wilson T. L., Gensheimer P., 2000, A&A, 358, 433
Martín S., Martín-Pintado J., Mauersberger R., 2006, A&A, 450, L13
Meijerink R., Spaans M., Israel F. P., 2006, ApJ, 650, L103
Negishi T., Onaka T., Chan K.-W., Roellig T. L., 2001, A&A, 375, 566
Oberst T. E. et al., 2006, ApJ, 652, L125
Rawlings J. M. C., Yates J. A., 2001, MNRAS, 326, 1423
Röllig M. et al., 2007, A&A, 467, 187
Rubin R. H., Simpson J. P., Haas M. R., Erickson E. F., 1991, ApJ, 374, 564
Schilke P., Carlstrom J. E., Keene J., Phillips T. G., 1993, ApJ, 417, L67
Seaquist E. R., Frayer D. T., 2000, ApJ, 540, 765
Sternberg A., Dalgarno A., 1995, ApJS, 99, 565
Tielens A. G. G. M., Hollenbach D., 1985, ApJ, 291, 747
Unger S. J. et al., 2000, A&A, 355, 885
Wild W., Harris A. I., Eckart A., Genzel R., Graf U. U., Jackson J. M., Russell A. P. G., Stutzki J., 1992, A&A, 265, 447
Wolfire M. G., Hollenbach D., Tielens A. G. G. M., 1989, ApJ, 344, 770
Wolfire M. G., Tielens A. G. G. M., Hollenbach D., 1990, ApJ, 358, 116
Wright E. L. et al., 1991, ApJ, 381, 200

This paper has been typeset from a TEX/LATEX file prepared by the author.